ADVANCED FUNCTIONAL MATERIALS
www.afm-journal.de

Self-Sacrifice Template Fabrication of Hierarchical Mesoporous Bi-Component-Active ZnO/$ZnFe_2O_4$ Sub-Microcubes as Superior Anode Towards High-Performance Lithium-Ion Battery

Linrui Hou, Lin Lian, Longhai Zhang, Gang Pang, Changzhou Yuan, and Xiaogang Zhang*

In the work, a facile yet efficient self-sacrifice strategy is smartly developed to scalably fabricate hierarchical mesoporous bi-component-active ZnO/$ZnFe_2O_4$ (ZZFO) sub-microcubes (SMCs) by calcination of single-resource Prussian blue analogue of $Zn_3[Fe(CN)_6]_2$ cubes. The hybrid ZZFO SCMs are homogeneously constructed from well-dispersed nanocrstalline ZnO and $ZnFe_2O_4$ (ZFO) subunites at the nanoscale. After selectively etching of ZnO nanodomains from the hybrid, porously assembled ZFO SMCs with integrate architecture are obtained accordingly. When evaluated as anodes for LIBs, both hybrid ZZFO and ZFO samples exhibit appealing electrochemical performance. However, the as-synthesized ZZFO SMCs demonstrate even better electrochemical Li-storage performance, including even larger initial discharge capacity and reversible capacity, higher rate behavior and better cycling performance, particularly at high rates, compared with the single ZFO, which should be attributed to its unique microstructure characteristics and striking synergistic effect between the bi-component-active, well-dispersed ZnO and ZFO nanophases. Of great significance, light is shed upon the insights into the correlation between the electrochemical Li-storage property and the structure/component of the hybrid ZZFO SMCs, thus, it is strongly envisioned that the elegant design concept of the hybrid holds great promise for the efficient synthesis of advanced yet low-cost anodes for next-generation rechargeable Li-ion batteries.

1. Introduction

Rechargeable lithium-ion batteries (LIBs), which are regarded as one of the most promising devices for energy storage and conversion, have attracted tremendous attention in the past decades.[1–4] As we all know, almost all the anodes of commercial LIBs are based on graphite-based materials, unfortunately, they still exhibit a relatively low Li-storage capacity of ≈372 mAh g^{-1} and potential safety issues as an anode,[5] which cannot meet the great demand of high-energy applications in current platforms, such as electric vehicles (EVs), hybrid EVs, electricity grid storage devices, and so on.[1–6] Therefore, it has become an urgent and significant task to extensively explore even higher capacity anode materials for the next-generation LIBs. Attractively, transition metal oxides (TMOs) stand out from versatile novel anode materials owing to their low cost, wide availability, and especially higher theoretical specific capacities (>600 mAh g^{-1}).[5,7–11] Furthermore, TMOs provide much more exciting choices to realize large reversible capacities via various ways involving alloying/dealloying processes, insertion/extraction mechanisms and/or conversion reactions.[1–4,12,14] Recently, fine assembly of two distinct TMOs into a hierarchical nanohybrids, particularly with highly homogenerous dispersion at the nanoscale,[9,14] would allow us to make the best of inherent interaction of each component for better electrochemical performance in LIBs, affording a fascinating avenue to finely tailor, and further generate highly promising anodes for high-performance LIBs.[5,9,13] Based on the appealing concept, a few of hybrid architectures constructed from different TMOs have been tentatively examined for LIBs, such as, Co_3O_4/Fe_2O_3,[5] $NiFe_2O_4/Fe_2O_3$,[8] $CoO/CoFe_2O_4$,[9] Fe_2O_3/MnO_2,[10] and $ZnO/ZnFe_2O_4$,[14] which all verify that these unique hybrid anodes are endowed with even better Li-storage performance (larger specific capacity, more stable cycling performance, etc.) than any single one.[5,8–10,13,14]

Prof. L. Hou, L. Lian, L. Zhang, Dr. G. Pang, Prof. C. Yuan
School of Materials Science and Engineering
Anhui University of Technology
Ma'anshan 243002, P.R. China
E-mail: ayuancz@ahut.edu.cn
Dr. G. Pang, Prof. X. Zhang
College of Material Science and Engineering
Nanjing University of Aeronautics and Astronautics
Nanjing 210016, P.R. China
Prof. C. Yuan
Chinese Academy of Science (CAS) Key Laboratory of Materials for Energy Conversion
Hefei 230026, P.R. China

DOI: 10.1002/adfm.201402827

In general, specific microstructure of electroactive materials is another important and unneglectable aspect determining the final Li-storage ability of an electrode,[4,12,13] besides the striking effect of multi-components mentioned above. As well established previously, unique robust micro-/nanostructures, as a unique higher-level secondary superstructure, typically of micro-/submicrometer dimensions but internally consisting of nano-building blocks and/or nanodomains, offer the exceptional advantages of both nanometer-sized building blocks/nano-domains and micro-/submicrometer-sized assemblies themselves.[4,5,14–17] In specific, the nano-scaled building blocks/nanodomains, with a large specific surface area (SSA) and a high surface-to-bulk ratio, offer negligible diffusion time and are the keys to favorable kinetics and high specific capacities. And the higher-level assemblies, with desirable mechanical properties and high tap density, guarantee good stability and practical fabrication.[4,18] In particular, when hierarchical micro-/nanostructures, especially with desirable mesoporosity, of hybrid hetero-components, were well constructed as expected, remarkable electrochemical performance then could be highly anticipated for advanced LIBs, owing to their rich lithium-storage sites, large electrode/electrolyte interfaces for high Li^+ flux across and/or absorption/desorption on the sur-/interfaces, reduced paths both for Li^+ ions and electrons diffusion.[4,5,19,20] Moreover, the typical mesoposity provides additional free volume to alleviate the structural strain associated with repeated Li^+-insertion/extraction processes to some extent, thus leading to an enhanced cycling ability even at large current rates.[4,5,17] Therefore, it is of both academic and practical importance in the LIB field to deeply understand how to further design and tailor hierarchical porous hybrids with outstanding Li-storage performacne at high rates.

Herein, ZnO and spinel bimetallic $ZnFe_2O_4$ (hereafter designed as ZFO) with high electrochemical activity via the combination of conversion reactions and dealloying-alloying of LiZn-Fe-Li_2O composite are selected as blocks to construct the hierarchical mesoporous hybrid with micro-/nanostructures, thanks to their large theoretical specific capacities (981 mAh g^{-1} for ZnO,[21,22] and 1072 mAh g^{-1} for ZFO,[4,23] high abundance, low toxitity, etc. However, it is commonly challengeable to build up an intergrated smart ZnO/$ZnFe_2O_4$ (henceforth denoted as ZZFO) architecture by exploring a simple but efficient approach, where structural features and electroactivities of each component are fully manifested, and the interface/chemical distributions are highly homogenerous at the nanoscale meanwhile. In the present, Prussian blue (PB) and Prussian blue analogues (PBAs) have been regarded as novel templates to prepare porous TMOs.[5,8,24–26] Compared with other templates, PB and/or PBAs template derived materials always exhibit large SSA, inter-connected mesopores, and uniform element distribution from inside to outside, and noticeably their morphologies and phase compositions can be rationally tuned by selecting suitable PB or PBA precursors. Unfortunately, up date to now, research into the fabrication of multiple TMO hybrids from the PB or PBAs, and further application as anode materials for high-performance LIBs are still at an early stage.

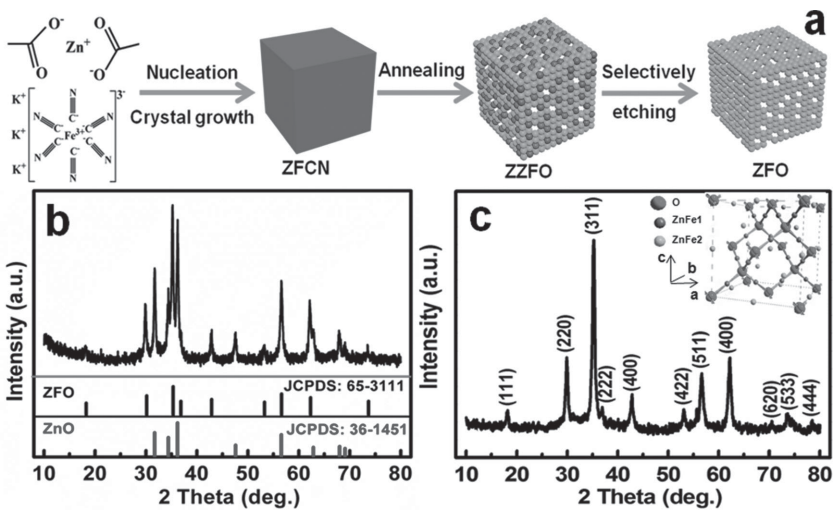

Figure 1. a) Schematic illustration of the self-sacrifice template synthetic process, typical wide-angle XRD patterns of the as-obtained b) ZZFO and c) ZFO products. The inset in panel (c) is for the representative crystallographic structure of the ZFO.

Based on the consideration and inspiration mentioned above, in this study, we reported a scalable bottom-up self-sacrifice template synthetic protocol to controllablly prepare hierarchical mesoporous ZZFO sub-microcubes (designed as SMCs), constructed by unique nanoparticle (NP) building blocks by the post-calcination of a typical single-resource PBA of $Zn_3[Fe(CN)_6]_2$ (henceforward denoted as ZFCN) precursor. Additionally, porously assembled ZFO SMCs were further obtained by following selectively chemical etching of the hierarchical hybrid ZZFO product. Benefiting from their appealing structural features, both of the ZZFO and ZFO SMCs delivered desirable electrochemical performance as high-performance anodes for LIBs. Impressively, the ZZFO anode possessed much better electrochemical Li-storage properties even at large current densities, thanks to its unique microstructure characteristics and striking synergistic effect between the bi-component-active, well-dispersed ZnO and ZFO nanophases at the nanoscale.

2. Results and Discussion

2.1. Synthesis and Structural Analysis of the As-Prepared ZZFO and ZFO SMCs

Herein, we rationally developed a self-sacrifice template synthetic strategy, which invloved facile yet scalable preparation of a PBA ZFCN template, following moderate calcination and selectively basic etching to controllably fabricate hierarchical porous ZZFO and ZFO SCMs, respectively, as schemetically illustrated in **Figure 1**a. As far as we know, lots of PBAs with various morphologies have been synthesized successfully, but some extra surfactants and/or high-temperature procedures are always necessary in all the fabricating strategies reported

before.[25–28] Herein, we first successfully put forward a simple bottom-up methodology for high-yield synthesis of typical ZFCN template in an ice-water bath, where no any surfactant is applied. Of particular note, this is of great signficance to large-scale industrial production. The crystallographic structure and phase purity of the as-obtained light yellow-green product (see Supporting Information, the inset in Figure S1) are examined by powder X-ray diffraction (XRD) measurement. All the presented diffraction peaks can be unambiguously assigned to the rhpmbohedra zinc iron cyanide (JCPDS No. 38–0688) with two types of octahedra ($Zn^{II}(NC)_6$ and $Fe^{III}(NC)_6$) (see Supporting Information, Figure S1a, b), and no any other impurities are observed. Of interest, when Co^{2+} is applied instead of Zn^{2+} in the synthetic procedure while other parameters keep the same, a new PBA of $Co_3[Fe(CN)_6]_2 \cdot 10H_2O$ (JCPDS No. 46–0907) still can be obtained (see Supporting Information, Figure S2a). In sharp contrast, just $KNi[Fe(CN)_6]$ (JSPDC No. 51–1897) is obtained for Ni^{2+} (see Supporting Information, Figure S2b), and even a unknown phase is prepared for the case of Mn^{2+} under the same conditions (see Supporting Information, Figure S2c). Also notably, all the three samples with irregular particle morphologies (see Supporting Information, Figure S3) are clearly observed when Co^{2+}, Ni^{2+} and Mn^{2+} are utilized instead of Zn^{2+} in the synthetic process. An extensive exploration into the underlying reasons for such distinct difference with various ions is undergoing.

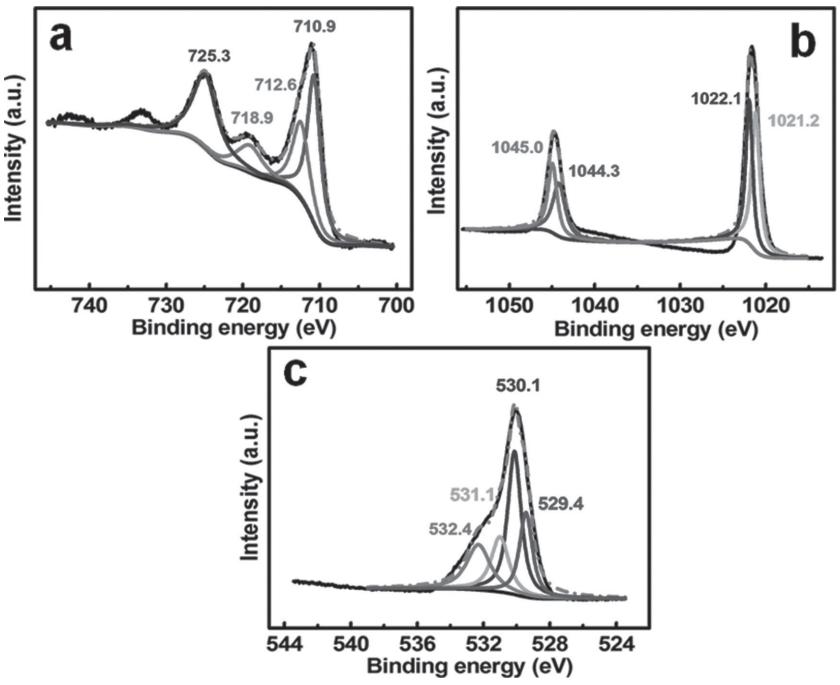

Figure 2. XPS survey spectra and fitted data of the as-obtained ZZFO sample: a) Fe 2p, b) Zn 2p, and c) O 1s.

An annealing treatment was further carried out at a moderate annealing temperature of 500 °C just for 2 h in air with a ramping rate of 1 °C min^{-1} to covert the resulting ZFCN phase into the mixed TMOs at the nanoscale, accompanying with the breakdown of Fe/Zn-CN and the gradual formation of Fe/Zn-O over annealing. As evident in the thermogravimetric analysis (TGA) data (see Figure S4, Supporting Information), a significant weight loss is of ≈43 wt% totally before complete decomposition, which should be attributed to the escape of absorbed water and organic molecules by the thermal decomposition of the ZFCN. The specific structure and phase of the annealed product are further investigated by XRD, and the corresponding wide-angle XRD reflections are demonstrated in Figure 1b, all the diffraction peaks reveal the two-phase coexistence of the cubic ZFO (JCPDS file no. 65–3111, Fd-sm(227)) and hexagonal ZnO (JCPDS file no. 36–1451, P63mc(186)) phases, suggesting the formation of the hybrid ZZFO composite. According to the known chemical composition of ZFCN, the corresponding XRD data for the products obtained at various annealing temperatures (see Figure S5, Supporting Information) and at 500 °C for different time (see Figure S6, Supporting Information), it is easy to conclude that the ZFO is gradually formed from the ZnO and Fe_2O_3 with the annealling temperature increasing. And the X-ray fluorescence spectrometry (XRFS) data further confirms the molar ratio of ZnO to ZFO in the final hybrid ZZFO is ≈2 : 1, that is, the ZZFO sample possesses high-content ZnO species of ≈40 wt%. Interestingly, after pyrolysis of $Co_3[Fe(CN)_6]_2 \cdot 10H_2O$ and $KNi[Fe(CN)_6]$, hybrid Co_3O_4/$CoFe_2O_4$ (see Figure S7a, Supporting Information) and NiO/$NiFe_2O_4$ (see Figure S7b, Supporting Information) are also expectedly fabricated, while a simple mixture of MnO_2, Mn_2O_3 and $Fe_{21.4}O_{32}$ is just obtained (see Figure S7c, Supporting Information) after annealling the product prepared by using Mn^{2+} instead of Zn^{2+} in the synthetic process.

Since ZnO is readily soluble in aqueous media at high pH condition,[29] the single ZFO is easily prepared through a basic etching of the hybrid ZZFO SMCs by 6 M NaOH solution for 5 h accordingly. As seen in Figure 1c, all the observed Bragg reflections peaks, not only including their peak positions but also intensities, can be successfully indexed to the bare ZFO phase (JCPDS file no. 65–3111, Fd-sm(227)) with spinel structure (the inset in Figure 1c) after chemically etching, and no peaks originated from other phase can be identified. The Zn and Fe species in the nanophase ZFO are both distributed over the tetrahedral (A) sites and octahedral (B) sites, commonly represented as $(Zn^{2+}_{1-x}Fe^{3+}_x)[Zn^{2+}_xFe^{3+}_{2-x}]O_4$,[30] as shown in the inset in Figure 1c. This find provides strong evidence for the completely selective elimination of ZnO phase from the hybrid ZZFO just by NaOH treatment at room temperature (RT) of 25 ºC.

The core level X-ray photoelectron spectra (XPS) and corresponding fitted data on the resultant ZZFO product in the Fe, Zn and O region are shown in **Figure 2**a-c, respectively. All the binding energies (BEs) in the XPS analysis are corrected for specimen charging by reflecting them to the C 1s peak (set at 284.6 eV). The Fe 2p spectrum, as seen in Figure 2a, is carefully fitted considering two spin-orbit doublets. The fitting peaks for

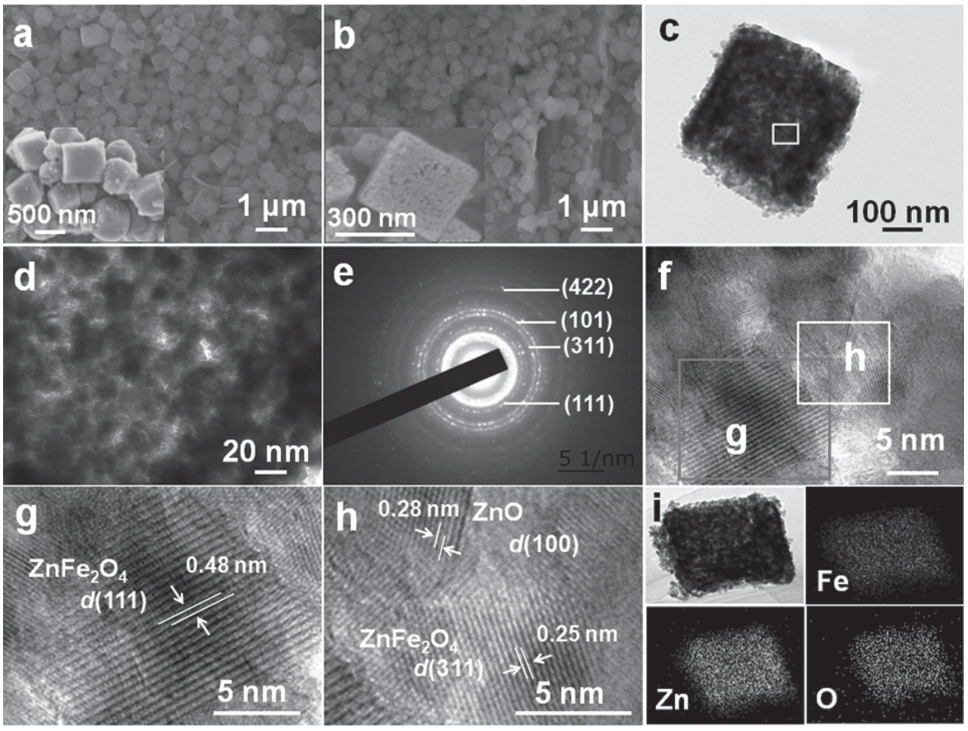

Figure 3. a) FESEM images of the precursor ZFCN; b) FESEM images, c,d) TEM images, e) SAED pattern and f–h) HRTEM images of the as-obtained ZZFO, i) elemental mapping images acted on an individual ZZFO cubic. The image in (d) is taken from the yellow rectangle region in the panel (c). The images in (g) and (h) are the magnified ones of the red and white rectangle regions in panel (f), respectively.

Fe $2p_{3/2}$ at BEs of ≈710.9 and ≈712.6 eV correspond well with tetrahedral (A-site) and octahedral (B-site) (the inset in Figure 1c), respectively. In addition, other peaks at BEs of ≈725.3 and ≈718.9 eV are in good agreement with the Fe $2p_{1/2}$ and the shake-up satellite structure, respectively, indicating the Fe (III) in the obtained ZZFO product.[31,32] The fitting results of the Zn 2p XPS spectrum are demonstrated in Figure 2b. The peaks at BEs of ≈1045.0 and ≈1022.1 eV can be attributed to Zn 2p1/2 and Zn 2p3/2, respectively, which reveals that the oxidation state of Zn is 2+ and is in good line with the spinel octahedral (B-site) in the present ZFO,[32,33] and we can also observe that another two peaks are located at BEs of ≈1021.2 and ≈1044.3 eV, and should be ascribed to the divalent Zn in the ZnO structure.[34] Furthermore, the high-resolution spectra of O 1s (Figure 2c) display a broad asymmetric curve, which can be deconvoluted into three peaks with BEs at ≈532.4, ≈530.1 and ≈529.4 eV, respectively. In specific, the distinctive peak at BE of ≈529.4 eV is assigned to typical lattice oxygen in the metal (Zn/Fe)-oxygen framework.[31,35,36] The peak at ≈530.1 eV suggests the presence of other O components (i.e., OH, H_2O or carbonate species) adsorbed on the NPs surface.[33] And the well-resolved peak sitting at BE of ≈532.4 eV corresponds to a higher number of defect sites with low oxygen co-ordination in the nano-scaled $ZnFe_2O_4$ and/or ZnO species.[35]

Figure 3a shows the panoramic field-emission scanning electron microscopy (FESEM) image of the as-fabricated ZFCN precursor. Numerous cube-shaped products with an size distribution ranged from ≈500 to ≈700 nm are obviously observed. Interestingly, when the precusor solution was kept at RT for 24 h during the synthetic procedure rather than at 4 °C in a refrigerator, some yellow irregular rod-shape products with unknown phase were surprisingly obtained instead (see Supporting Information, Figure S8). This observation strongly indicates the low temperature of 4 °C played a great role in formation of pure ZFCN precursor. And the underlying intrinsic formation mechanism is exlpored in our Lab. The closer inspection (the inset in Figure 3a) demonstrates that the surface of the PBA ZFCN SMCs is rather smooth. Typical low-resolution FESEM images of the ZFCN-derived ZZFO products by annealing at 500 °C with a temperate ramp of 1 °C min^{-1} are displayed in Figure 3b. Apparently, the as-obtained ZZFO inherits well original cube-like morphology of the precursor ZFCN without noticable size change and calcination-induced significant alterations. As a sharp contrast, close-up views reveal that the resultant ZZFO presents a relatively rough surface decorated with numerous tiny holes on their surface (the inset in Figure 3b). Of note, when calcinated with a higher ramping rate of 5 °C min^{-1}, the structure of the ZZFO is wholly collapsed (see Supporting Information, Figure S9). Thus, the heating rate plays another significant role in retaining the unique mesoprous SCM structure. Transmission electron microscopy (TEM) microscopic method was further carried out to clucidate the specific morphology and microstructure of the as-synthesized ZZFO more detailedly. The brighter contrast in low-resolution TEM image (Figure 3c) demonstrates the extremely porous nature of the resulting ZZFO itself. As expected, thermal decomposition takes palce during the calcination in air, and generates gas products like CO_2 and NO_2 which escape from the inside of the precursor of ZFCN, thus giving rise to the formation of loosely porous ZZFO SMCs. A

magnifying TEM image (Figure 3d), detected from a sampling area indicated by the yellow rectangle region in Figure 3c, further reveals that the unique porous ZZFO is really composed of numerous interconnected primary NP building blocks of ≈10–15 nm in size, whereby a large number of pores of ≈3–7 nm in size are left between adjacent nanocrystallites. This appealing structural feature would greatly favor for obtaining much more electroactive sites for efficient electrochemical energy storage, and provide more convenient mass transport meanwhile. The selected area electron diffraction (SAED) pattern (Figure 3e) with a series of concentric rings reveals the polycrystalline characteristics of the ZZFO, and matches well with (111), (311), (422) planes of the ZFO, and (101) planes of the ZnO, respectively. This is in good correspondence with the XRD characterization results described above (Figure 1b). High-resolution TEM (HRTEM) visualizations (Figure 3f–h) further demonstrate that the well-developed NP subunits are attached with each other in various orientations, despite displaying clear lattice fringes. As observed in Figure 3g, which is taken from the red rectangle region in Figure 3f, clear littice fringes can be seen obviously with a spacing of ≈0.48 nm, corrsponding to the interplanar distance of (111) crystalline plane of the spinel ZFO. Further examination (Figure 3h), corresponding to the magnified white square zero in Figure 3f, clearly demonstrates well-defined lattice finges in two regions with the spacing are ≈0.28 and ≈0.25 nm, respectively, which can be attributed to the (100) crystalline plane of the ZnO and the (311) facet of ZFO phase. This observation strongly suggests that the two phases of ZnO and ZFO even with heterojunction nanostrucutre are well dipersed at the nanoscale. As for the chemical composition/component and elemental distribution of the ZZFO, Figure 3i further gives a typical TEM energy dispersive spectrometer (EDS) elemental mapping analysis of a single ZZFO SMC, evidently revealing the extremely homogeneous co-existence and uniform distribution of Fe, Zn and O species from inside to outside in the whole ZZFO cube.

Strikingly, after selectively etching of the high-content ZnO existing in the hybrid ZZFO product, the hierarchical cubic structure of submicro size is still noticeably retained with good structural integrity (**Figure 4**a and b), and no occurrence of etching-induced structure collapsion is observed, evidently verifying the robust structural stability of the as-prepared ZFO SMCs. Furthermore, as seen in the TEM images (Figure 4b and **c**), highly porous architecture assembled by lots of nano-scaled NP buinding blocks is apparently presented. The SAED pattern (the inset in Figure 4c) comprising well resolved clear set of concentric rings with occasional bright spots, apparently suggests the nanocrystalline nature of the as-obtained ZFO. And further closer inspection on the HRTEM image (Figure 4d) clearly confirms the lattice finge of (311) crsytal plane with interplane distance of ≈0.25 nm (the inset in Figure 4d) for the ZFO phase.

The Brunauer–Emmett–Teller (BET) SSA and specific pore structure of the hybrid ZZFO and the derivative of ZFO were comparatively probed with N_2 adsorption-desorption isotherm measurements at a temperature of 77 K, and the derived structural parameters are also collected exhaustively (see Table S1, Supporting Information). As plotted in **Figure 5**a, both of the isotherms of the ZZFO

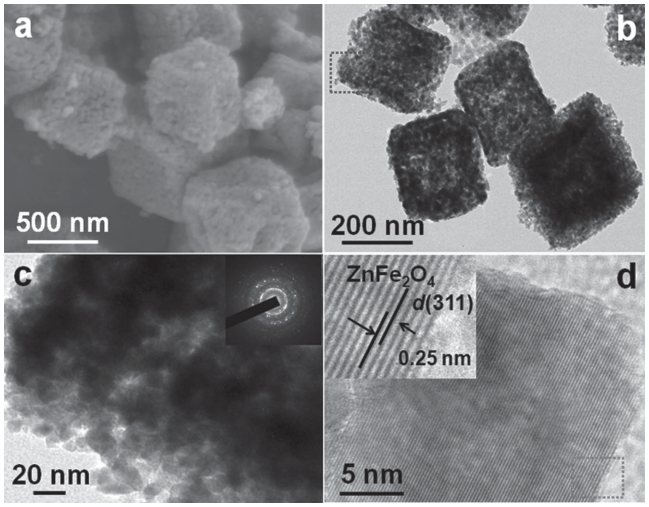

Figure 4. a) FESEM image, b,c) TEM images, SAED pattern (the inset in panel c) and d) HRTEM image of the as-obtained ZFO. The image (c) is taken from the blue rectangle region in the panel (b). The inset image in (d) is taken from the region marked with the red rectangle in panel (d).

and ZFO samples are similar to each other and can be classified as type IV,[7,37,38] according to the International Union of Pure and Applied Chemistry (IUPAC) classification, possessing a distinct H3-type hysteresis loop at a relative pressure ranges of 0.69–1.0 (ZFO) and 0.57–1.0 (ZZFO) P/P_0, repectively, which indicates the typical mesoporous characteristics of both the two SMCs. Remarkably, a shift of adsorption step and hysteresis loop towards higher relative pressure observed for the ZFO, compared to that of the hybrid ZZFO, reveals much more porosity and larger pore size for the ZFO sample,[37,39] resuting in notably expanded SSA of ≈66.2 m^2 g^{-1} and larger pore volume of 0.2 m^3 g^{-1} for the ZFO owing to the selectively chemical elimination of the co-exsting nanosized ZnO. As a contrast, the fitting analysis with BET equation shows a lower SSA of ≈54.3 m^2 g^{-1} and pore volume of 0.14 m^3 g^{-1} just for the ZZFO. Futherrmore, the average pore size of the ZZFO is calculated as ≈9.2 nm by the Barrett–Joyner–Halenda (BJH) method, smaller than that of 11.1 nm for the ZFO. The enlarged pore size after bacically etching also can be further confirmed by the pore size distribution (PSD) curves in Figure 5b.

Benefiting from these intriguing structural features described above, the unique hierarchical porous ZZFO and

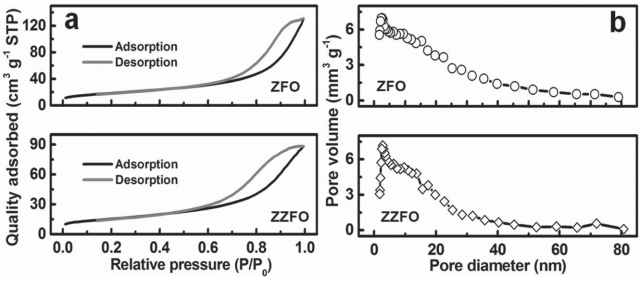

Figure 5. a) N_2 adsorption-desorption isotherms and b) PSD data of the as-prepared ZZFO and ZFO products as indicated.

ZFO SMCs constructed by fine NP subunits guarantee desirable accommodation of the strain during the Li^+ insertion/removal, large electrode/electrolyte contact surface, short and convenient diffusion paths for ionic transport, appealing mechanical properties, relatively high tap density (≈0.78 g cm^{-3} for ZZFO; ≈0.71 g cm^{-3} for ZFO), and good stability, which would be greatly meaningful for the huge enhancement of the electrochemical performance as anode materials for practical application in advanced LIBs. Moreover, with regard to the ZZFO, owing to the well-dispersed bi-component-active ZnO and ZFO nanophases at the nanoscale, even better electrochemical lithium-storage performance can be eagerly expected.

2.2. Electrochemical Performance of Hierarchical Mesoporous ZZFO and ZFO SMCs

Electrochemical performance of the hierarchical mesoporous ZZFO and ZFO SMC anodes were next examined by means of galvanostatic discharge-charge (i.e., Li insertion-extraction) experiments by using the standard ZZFO (or ZFO)/Li half-batteries at RT. **Figure 6**a shows typical profiles for the voltage versus capacity of the first, second and third cycles of the synthesized samples, respectively, at a large current rate of 1000 mA g^{-1} in the potential range from 0.01 to 3.0 V with Li foil as a counter electrode. In the first discharge process, both of the ZZFO and ZFO anodes exhibit similar profiles with two small voltage plateaus at ≈1.42 and ≈0.95 V, and a clear long flat plateau at ≈0.8 V. As for the subsequent discharge process, the potential plateau shifts upward to ≈1.0 V due to structural reorganization, new phase formation and a polarization change in the electrode material.[8,40,41] As seen in Figure 6a, the initial discharging specific capacity of the ZZFO anode is ≈1892 mAh g^{-1}, even higher than its theoretical capacity (≈1027 mA g^{-1} = 981 mAh g^{-1} × 40 wt% (ZnO) + 1072 mAh g^{-1} × 60 wt% (ZFO)), while the first discharging capacity of 854 mA g^{-1} for the single ZFO at the same rate, which should be attributed to the extra contribution of the high-content nanophase ZnO (even an initial capacity of ≈2300 mAh g^{-1} observed for nanosized ZnO[21] in the hybrid, the decomposition of the electrolyte to form a solid electrolyte interphase (SEI) layer on the surface of the hybrid anode, as well as other factors, such as the intrinsic nature of the materials and kinetic limitations,[7,10,42] and maybe the synergistic effect of the two (i.e., "1 + 1 ≥ 2").[43] Remarkably, the initial discharge capacity of the ZZFO SMCs demonstrated here is much larger than those for other composite anodes, such as, Fe_2O_3/MnO_2 (≈1480 mA g^{-1}),[10] Co_3O_4/Fe_2O_3 (≈1687 mAh g^{-1}),[5] $NiFe_2O_4/Fe_2O_3$ (≈1401 mAh g^{-1}),[8] $CoO/CoFe_2O_4$ (≈1285 mAh g^{-1}),[9] $ZnO/ZnFe_2O_4$ (≈650 mA g^{-1}),[14] and even other $ZnFe_2O_4$ samples (≈1400 mAh g^{-1}).[44,45] The first charge (i.e., de-lithiation) curve of the ZZFO anode illustrates the lithium extraction, in which a stead and smooth voltage increase from 0.01 to 3.00 V, and the overall charging capacity is ≈1371 mAh g^{-1}. As a consequency, there is an irreversible capacity loss of ≈521 mAh g^{-1} between the first discharge and charge cycles, accordingly, the initial Coulombic efficiency (CE) is ≈70%, very close to that of the single ZFO anode (≈72%). The second-discharge profile of the ZZFO anode still shows a high capacity of ≈1405 mA g^{-1}, and the second-charge curve resembles the first-charge one but shows slightly low capacity value (≈1249 mAh g^{-1}) and a higher plateau voltage. The subsequent discharge/charge profiles exhibit qualitative resemblance to that of the 2nd cycle curves except for the gradually decreasing capacities. Surprisingly, we note that the ZFO with a much larger SSA delivers a smaller specific capacity, which is in marked contrast to the ZZFO with lower SSA. It reveals that the electrochemical Li-storage performance of the ZZFO is associated more dierctly with structure and component aspects than its SSA. The differences between the ZZFO and ZFO mainly lie in the existence of extra ZnO phase well-dispered in the hybrid ZFFO, and smaller pore size and volume meanwhile for the ZZFO product. Therefore, it is easily spectulated that synergetic effect of the ZnO and ZFO cannot be ignored at all, additionally, relatively approperiate pore structure should be more convient and accessible for electrolyte diffusion and Li^+ into the electroactive phases, thereby rendering better electrochemical properties of the ZZFO. Besides the higher initial capacity and desirable CE, outstanding rate capability also can be observed for the hybrid ZZFO anode. Figure 6b shows the rate capability of the ZZFO and ZFO at progressively increased current densities ranged from 100 to 2000 mA g^{-1}. Attractively, the ZZFO exhibits decent capacity retention with an average discharge capacities of ≈1197, ≈950, ≈839, ≈728, ≈688 mAh g^{-1} at current densities of 100, 200, 500, 1000, and 1500 mAh g^{-1}, respectively. Even at a rigiously high rate of 2000 mA g^{-1}, a large discharge capacity of ≈667 mAh g^{-1} still could be imparted, which indicates that ≈56% of the capacity is even maintained when the current rate is increased from 100 to 2000 mA g^{-1}. More significantly, a high discharge capacity of ≈1073 mAh g^{-1} is recovered when the current density is returned to 100 mA g^{-1}. By contrast, the bare ZFO only can deliver ≈744, ≈629, ≈490, ≈380, ≈287, ≈222 mAh g^{-1} at the current densities of 100, 200, 500, 1000, 1500, and 2000 mA g^{-1}, respectively, that is, the specific capacity of the ZFO anode just retains as ≈30% as the rate is up to 2000 from 100 mA g^{-1}. And only an average capacity of ≈583 mAh g^{-1} can be recovered when the current density is further reduced stepwise to 100 mA g^{-1}, as evidence in Figure 6b. The

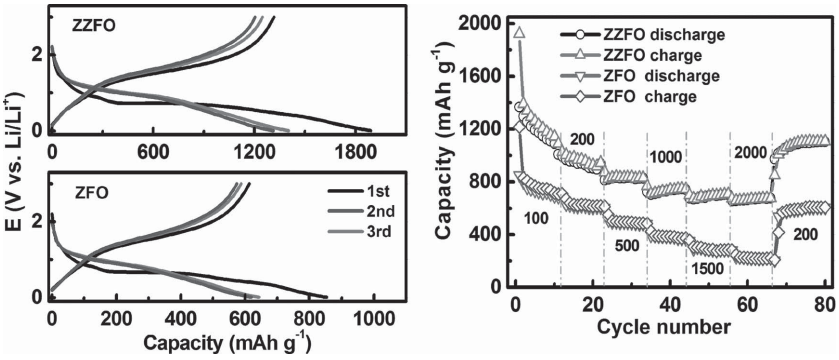

Figure 6. Electrochemical properties of the as-fabricated ZZFO and ZFO as anodes in LIBs: a) discharge-charge voltage profiles at a current density of 1000 mA g^{-1}, b) rate capability at various current rates ranged from 100 to 2000 mA g^{-1} as indicated

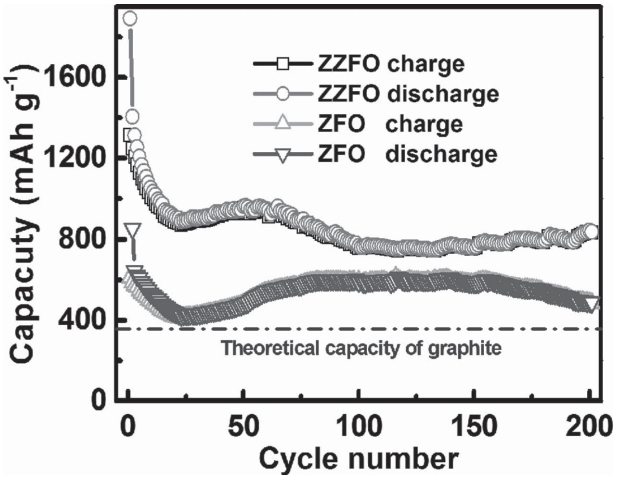

Figure 7. Cycling performance of the mesoporous ZZFO and ZFO electrodes at a current density of 1000 mA g^{-1} as a function of cycle number as indicated

above-mentioned data obviously highlights much better rate performance and larger capacity retention of the ZZFO than those for ZFO under the same rate, which can be further verified by the electrochemical impedance spectroscopy (EIS) data (see Figure S10, Supporting Information) and corresponding fitted results (see Table S2, Supporting Information). Furthermore, the charge capacities are overlapped well with discharge counterparts both for the ZZFO and ZFO anodes, confirming the good electrochemical reversibility of the two anodes, as shown in Figure 6b.

In addition to a large specific capacity and excellent rate behavior, cycling performance is another crucial property for high-performance LIBs, particularly at high rates. **Figure 7** comparatively depicts the capacity vs the cycle number profiles for the ZZFO and ZFO anodes, respectively, at a large current density of 1000 mA g^{-1} in the potential range of 0.01 to 3.0 V (vs Li/Li^+). It is worthy of noting that the discharge capacity decreases rapidly during the first dozens of cycles for both of the ZZFO and ZFO anodes, and thereafter, the specific capacity begins to grow significantly then, which is normally observed for TMO-based anodes. This phenomenon is generally attributed to the reversible formation of a polymeric gel-like film originating from kinetic activation in the electrode.[15,46–48] More impressively, the discharge capacity of the ZZFO remains relatively stable after continuously cycling for ≈100 times, and is even kept as high as ≈837 mAh g^{-1} over 200 cycles. As seen from the FESEM and TEM images of the ZZFO anode after 200 cycles at the current rate of 1000 mA g^{-1}, some SMCs still can be evident (see Figure S11, Supporting Information), suggesting its desirable structural stability over cycling, which should be well responsible for the excellent cycling performance. For comparison purpose, the ZFO anode exhibits a rapid decay in its capacity, and just a specific capacity of ≈487 mAh g^{-1} is left after 200 cycles under identical test conditions, nevertheless, the capacity is still much higher than the theoretical value of common commercial graphite (≈372 mAh g^{-1}) ,[5] as plotted in Figure 7. More importantly the ZZFO SMCs still remain a large reversible capacity of ~701 mAh g^{-1} after 200 charge–discharge cycles even at a higher current density of 2000 mA g^{-1}, in stark contrast to that of the ZFO, whose specific capacity only maintains as ≈453 mAh g^{-1} (see Figure S12, Supporting Information). As a result, it is easy to conclude that the specific capacity of the ZZFO anode can be excellently preserved after a long-term cycling even under large current rates. Moreover, during the cycling for the first 30 times at 2000 mA g^{-1}, although the ZZFO anode exhibits lower CE than that of ZFO, both of the two then retain high CE of ~98% in the sequent cycles (see Figure S13, Supporting Information), suggesting their desirable CE over continuously cycling for 200 times. More strikingly, as for higher loading (≈1.3 mg) of ZZFO per Cu foil, the ZZFO anode still can maintain a large capacity of ≈590 mAh g^{-1} after cycling for 150 times at a current rate of 1000 mA g^{-1} (see Figure S14, Supporting Information), which is greatly meaningful for the practical applications. The good cycling behaviors of the ZZFO and ZFO SMCs should be partially ascribed to their hierarchical porous SMC structures, which ensure the presence of the additional free volume to alleviate the structural strain associated with repeated Li^+ insertion/extraction processes.[2–4,19] As established well before,[14,21,49,50] the ZnO itself is the electrochemically active anode for Li^+ storage, however, it seriously suffers from its poor cycling performance owing to its poor conductivity and severe pulverization, and commonly turns out to be electrochemically inactive after several cycles. Thus, as for the ZZFO anode here, it is worth mentioning that one thing must not be overlooked that the significant roles played by the homogeneously dispersed ZnO phase in the enhanced cycling behavior of the hybrid ZZFO SMCs, taking its outstanding cycling performance, even better than the single ZFO anode (see Figure 7), into account. High-content symbiotic ZnO in the hybrid, as well-dispersed buffer domains, can efficiently and spatially separate the coexisting highly electroactive ZFO phase at the nanoscale, and further prevent the self-aggregation of nanophase ZFO during following continuous cycles, strongly favoring for the enhanced cycling performance of the ZZFO anode. Furthermore, the formation of the uniform hybrid ZZFO SMCs from the nanophase ZFO and ZnO also can relieve the crystal strain of each electrode domains caused by the volume change during electrochemically cycling.[28,51] It is the above-described synergistic effect of the two that results in the higher electrochemical stability of the hierarchical porous ZZFO SMCs even at high rates.[9,14]

3. Conclusions

In summary, hierarchical hybrid electrodes elegantly designed in component and structure are highly desirable for the huge development of advanced lithium-ion batteries (LIBs), as they can take full advantage of diverse components and various microstructures to stably deliver superior Li-storage performance at high rates. Herein, hierarchical mesoporous bi-component-active $ZnO/ZnFe_2O_4$ (ZZFO) sub-microcubes (SMCs), constructed from nanocrystalline particle building blocks of ≈15 nm, were rationally prepared via efficient self-sacrifice template strategy by annealing single-resource Prussian blue analogue of $Zn_3[Fe(CN)_6]_2$ cubes. The two phases of ZnO and $ZnFe_2O_4$ (ZFO) were homogeneously dispersed at the nanoscale in the hybrid ZZFO SMCs. The following selectively basic etching of ZnO nanodomains from the hybrid yielded porously assembled ZFO SMCs. When utilized as attractive anodes for LIBs, both of ZZFO and ZFO products exhibited appealing electrochemical performance. As a sharp contrast,

the resultant ZZFO SMCs delivered electrochemical lithium-storage properties superior to those of the single-phase ZFO anode, which should be reasonably attributed to its unique microstructure characteristics and striking synergistic effect between the bi-component active, well-dispersed ZnO and ZFO phases at the nanoscale. Moreover, the insights into the correlation between the electrochemical Li-storage properties and the structure/component of the hybrid ZZFO SMCs is significantly favorable for further rational design, and efficient synthesis of the advanced hybrid anodes for next-generation LIBs in the future.

4. Experimental Section

Synthesis of the $Zn_3[Fe(CN)_6]_2$ Precursor: All the chemicals used in this study were analytic-grade reagents and used directly without further purification. In a typical synthesis of the precursor ZFCN, 0.329 g of $K_3Fe(CN)_6$ was dissolved into 60 mL of de-ionized (DI) water to form a transparent solution firstly (solution A). Then, 0.329 g of $Zn(CH_3COO)_2{\cdot}2H_2O$ is dissolved into another 20 mL of DI water to form a transparent solution (solution B). The two solutions were both transferred to an ice bath. After stirred for 10 min, the solution B was taken out from the ice bath, and then added into the solution A drop by drop under vigorously stirred in ice bath. After further stirred in ice bath for another 2 h, the mixed solution was transferred into a refrigerator, keeping at 4 °C in a refrigerator for 24 h. Then, the precipitate was filtered, and washed several times with DI water and absolute ethanol for several times, respectively. After dried for 24 h, the light yellow-green product (see Supporting Information, the inset Figure S1) was obtained. For comparison, the mixed solution was kept at room temperature (RT) for 24 h instead; accordingly, yellow sample was prepared (see Supporting Information, the inset Figure S8c). In addition, $Co(CH_3COO)_2{\cdot}4H_2O$, $Ni(CH_3COO)_2{\cdot}4H_2O$ and $Mn(CH_3COO)_2{\cdot}4H_2O$ were applied, respectively, to fabricate other precursors while other synthetic parameters were kept the same to that of $Zn(CH_3COO)_2{\cdot}2H_2O$.

Synthesis of the ZZFO and ZFO Products: The as-synthesized ZFCN was annealed in air at a temperature of 500 °C for 2 h in an electric oven with a temperate ramp of 1 °C min^{-1} in order to synthesize ZZFO CMCs sample. For comparison purpose, another temperate ramp of 5 °C min^{-1} was also applied instead. And single-phase ZFO product was obtained by selectively etching the as-prepared ZZFO by using 6 M NaOH solution under stirred for 6 h at RT.

Characterization of Materials: The samples were examined by powder X-ray diffraction (XRD) (Bruker, D8-Advance XRD, Germany) by using a Cu K*a* source (λ = 0.154056 nm) at a scanning speed of 2° min^{-1} over a 2θ range of 10–80°. The morphologies and structures were observed with field-emission scanning electron microscopy (FESEM, JEOL-6300F, 15 kV), transmission electron microscope (TEM), high-resolution transmission electron microscope (HRTEM), and selected area electron diffraction (SAED) (JEOL JEM 2100 system operating at 200 kV). Thermogravimetric analysis (TGA) was carried out under air flow with a temperature ramp of 10 °C min^{-1}. N_2 adsorption/desorption isotherms were determined by Brunauer–Emmett–Teller (BET) measurement by using an ASAP-2010 surface area analyzer. The pore size distribution (PSD) was derived from the adsorption branch of the Barrett–Joyner–Halenda (BJH) method. X-ray photoelectron spectroscopy (XPS) measurements were performed on a PHi5000 X-ray photoelectron spectrometer with an Al K*a* excitation source (1486.6 eV), the spectra were fitted with the XPSPEAK41 software. The element analysis was carried out by X-ray fluorescene spectrometer (XRFS, ARL Advant'X 3600).

Electrochemical Measurements: The working electrode consisted of the electroactive ZZFO or ZFO samples, conductive material (acetylene black, Super-P-Li), and sodium carboxymethyl cellulose (CMC, average M_w: ≈250 000) at a weight ratio of 70 : 20 : 10 with water as a solvent upon the copper foil substrate. The resultant slurry was uniformly spread onto pure Cu foil using a doctor blade, and dried at 110 °C for 12 h. The average loading of electroactive ZZFO or ZFO is ≈0.9 mg per Cu foil, and the thickness of each electrode is ≈4.8 μm (see Figure S15, Supporting Information). For comparison, the ZZFO anode with higher loading (≈1.3 mg) per Cu foil was also prepared. CR2016-type coin cells were fabricated by sandwiching a porous polypropylene separator between the working electrode and Li metal foil (Cyprus Foote Mineral, 99.98%, USA) in a high-purity Ar-filled glove box with both the moisture and the oxygen content below 1 ppm. The electrolyte used here was 1 M $LiPF_6$ in a mixed solvent of ethylene carbonate (EC), dimethylcarbonate (DMC) and diethyl carbonate (DEC) (1 : 1 : 1, V/V/V) as the electrolyte. Galvanostatic discharge-charge cycling performance of the cells was conducted by using a CT2001A tester (Wuhan, China) at different rates as indicated between cut-off potentials of 0.01 and 3.0 V (vs Li/Li^+). Electrochemical impedance spectroscopy (EIS) measurements were performed with an IVIUM electrochemical workstation (the Netherlands).

Supporting Information

Supporting Information is available from the Wiley Online Library or from the author.

Acknowledgments

This work is partly supported by the National Natural Science Foundation of China (no. 51202004), the Nature Science Foundation of Anhui Province (no. KJ2013A051), the Opening Project of CAS Key Laboratory of Materials for Energy Conversion (no. 2014001), and the Graduate Innovation Program of Anhui University of Technology (no. 2013008, 2013009).

Received: August 18, 2014
Revised: October 26, 2014
Published online: November 19, 2014

[1] M. Armand, J. M. Tarascon, *Nature* **2008**, *451*, 653.
[2] P. G. Bruce, B. Scrosati, J. M. Tarascon, *Angew. Chem. Int. Ed.* **2008**, *47*, 2930.
[3] P. Poizot, F. Dolhem, *Energy Environ. Sci.* **2011**, *4*, 2003.
[4] C. Z. Yuan, H. B. Wu, Y. Xie, X. W. Lou, *Angew. Chem. Int. Ed.* **2014**, *53*, 1488.
[5] Z. Q. Li, B. Li, L. W. Yin, Y. X. Qi, *ACS Appl. Mater. Interfaces* **2014**, *6*, 8098.
[6] M. R. Palacín, *Chem. Soc. Rev.* **2009**, *38*, 2565.
[7] S. L. Xiong, J. S. Chen, X. W. Lou, H. C. Zeng, *Adv. Funct. Mater.* **2012**, *22*, 861.
[8] G. Huang, F. F. Zhang, L. L. Zhang, X. C. Du, J. W. Wang, L. M. Wang, *J. Mater. Chem. A* **2014**, *2*, 8048.
[9] M. X. Li, Y. X. Yin, C. J. Li, F. Z. Zhang, L. J. Wan, S. L. Xu, D. G. Evans, *Chem. Commun.* **2012**, *48*, 410.
[10] X. Gu, L. Chen, Z. C. Ju, H. Y. Xu, J. Yang, Y. T. Qian, *Adv. Funct. Mater.* **2013**, *23*, 4049.
[11] P. Poizot, S. Laruelle, S. Grugeon, L. Dupont, J. M. Tarascon, *Nature* **2000**, *407*, 496.
[12] L. Zhang, H. B. Wu, X. W. Lou, *Adv. Energy Mater.* **2014**, *4*, 1300958.
[13] H. B. Wu, J. S. Chen, H. H. Hng, X. W. Lou, *Nanoscale* **2012**, *4*, 2526.
[14] M. A. Woo, T. W. Kim, I. Y. Kim, S. J. Hwang, *Solid State Sci.* **2011**, *182*, 91.
[15] C. Z. Yuan, J. Y. Li, L. H. Zhang, L. R. Hou, X. G. Zhang, *Part. Part. Syst. Charact.* **2014**, *31*, 657.

[16] C. Z. Yuan, J. Y. Li, L. R. Hou, J. D. Lin, G. Pang, L. H. Zhang, X. G. Zhang, *RSC Adv.* **2013**, *3*, 18573.
[17] Z. Y. Wang, L. Zhou, X. W. Lou, *Adv. Mater.* **2012**, *24*, 1903.
[18] C. Z. Yuan, X. G. Zhang, L. H. Su, B. Gao, L. F. Shen, *J. Mater. Chem.* **2009**, *19*, 5772.
[19] A. S. Aricò, P. Bruce, B. Scrosati, J. M. Tarascon, A. V. Schalkwijk, *Nat. Mater.* **2005**, *4*, 366.
[20] R. B. Wu, X. K. Qian, K. Zhou, J. Wei, J. Lou, P. M. Ajayan, *ACS Nano* **2014**, *8*, 6297.
[21] S. J. Yang, S. Nam, T. Kim, J. H. Im, H. Jung, J. H. Kang, S. G. Wi, B. Park, C. R. Park, *J. Am. Chem. Soc.* **2013**, *135*, 7394.
[22] S. M. Abbas, S. T. Hussain, S. Ali, N. Ahmad, N. Ali, A. Abbas, *J. Mater. Sci.* **2013**, *48*, 5429.
[23] A. Varzi, D. Bresser, J. V. Zamory, F. Müller, S. Passerini, *Adv. Energy Mater.* **2014**, DOI:10.1002/aenm.201400054.
[24] P. Nie, L. F. Shen, H. F. Luo, B. Ding, G. Y. Xu, J. Wang, X. G. Zhang, *J. Mater. Chem. A* **2014**, *2*, 5852.
[25] N. Yan, L. Hu, Y. Li, Y. Wang, H. Zhao, X. Y. Hu, X. K. Kong, Q. W. Chen, *J. Phys. Chem. C* **2012**, *116*, 7227.
[26] L. Zhang, H. B. Wu, S. Madhavi, H. H. Hng, X. W. Lou, *J. Am. Chem. Soc.* **2012**, *134*, 17388.
[27] L. Hu, P. Zhang, Q. W. Chen, N. Yan, J. Y. Mei, *Dalton Trans.* **2011**, *40*, 5557.
[28] L. Hu, P. Zhang, Q. W. Chen, J. Y. Mei, N. Yan, *RSC Adv.* **2011**, *1*, 1574.
[29] L. Zou, F. Li, X. Xiang, D. G. Evans, X. Duan, *Chem. Mater.* **2006**, *18*, 5852.
[30] M. J. Akhtar, M. Nadeem, S. Javaid, M. Atif, *J. Phys.: Condens. Matter.* **2009**, *21*, 405303.
[31] Y. Sharma, N. Sharma, G. V. Subba Rao, B. V. R. Chowdari, *Electrochim. Acta* **2008**, *53*, 2380.
[32] M. Wang, Z. Ai, L. Zhang, *J. Phys. Chem. C* **2008**, *112*, 13163.
[33] H. J. Lv, L. Ma, P. Zeng, D. N. Ke, T. Y. Peng, *J. Mater. Chem.* **2010**, *20*, 3665.
[34] X. H. Liu, J. Zhang, L. W. Wang, T. L. Yang, X. Z. Guo, S. H. Wu, S. R. Wang, *J. Mater. Chem.* **2011**, *21*, 349.
[35] C. Z. Yuan, J. Y. Li, L. R. Hou, J. D. Lin, X. G. Zhang, S. L. Xiong, *J. Mater. Chem. A* **2013**, *1*, 11145.
[36] C. Z. Yuan, J. Y. Li, L. R. Hou, X. G. Zhang, L. F. Shen, X. W. Lou, *Adv. Funct. Mater.* **2012**, *22*, 4592.
[37] K. S. W. Sing, D. H. Everett, R. A. W. Haul, L. Moscou, R. A. Pierotti, J. Rouquérol, T. Siemieniewska, *Pure Appl. Chem.* **1985**, *57*, 603.
[38] C. Z. Yuan, J. Y. Li, L. R. Hou, L. Yang, L. F. Shen, X. G. Zhang, *J. Mater. Chem.* **2012**, *22*, 16084.
[39] Y. Y. Lü, W. W. Zhan, Y. He, Y. T. Wang, X. J. Kong, Q. Kuang, Z. X. Xie, L. S. Zheng, *ACS Appl. Mater. Interfaces* **2014**, *6*, 4186.
[40] C. Y. Wu, X. P. Li, W. S. Li, B. Li, Y. Y. Wang, Y. T. Wang, M. Q. Xu, L. D. Xing, *J. Power Sources* **2014**, *251*, 85.
[41] Z. C. Bai, Z. C. Ju, C. L. Guo, Y. T. Qian, B. Tang, S. L. Xiong, *Nanoscale* **2014**, *6*, 3268.
[42] R. Dedryvère, S. Laruelle, S. Grugeon, P. Poizot, D. Gonbeau, J. M. Tarascon, *Chem. Mater.* **2004**, *16*, 1056.
[43] C. Z. Yuan, L. H. Zhang, L. R. Hou, G. Pang, X. G. Zhang, *Part. Part. Syst. Charact.* **2014**, *31*, 778.
[44] Z. Xing, Z. C. Ju, J. Yang, H. Y. Xu, Y. T. Qian, *Nano Res.* **2012**, *5*, 477.
[45] Y. Ding, Y. F. Yang, H. X. Shao, *Electrochim. Acta* **2011**, *56*, 9433.
[46] S. Laruelle, S. Grugeon, P. Poizot, M. Dolle, L. Dupont, J. M. Tarascon, *J. Electrochem. Soc.* **2002**, *149*, A627.
[47] J. F. Li, S. L. Xiong, X. W. Li, Y. T. Qian, *Nanoscale* **2013**, *5*, 2045.
[48] J. F. Li, S. L. Xiong, Y. R. Liu, Z. C. Ju, Y. T. Qian, *ACS Appl. Mater. Interfaces* **2014**, *6*, 3268.
[49] X. H. Huang, R. Q. Guo, J. B. Wu, P. Zhang, *Mater. Lett.* **2014**, *122*, 82.
[50] X. H. Huang, X. H. Xia, Y. F. Yuan, F. Zhou, *Electrochim. Acta* **2011**, *56*, 4960.
[51] S. M. Park, E. J. Yoo, I. Honma, *Nano Lett.* **2009**, *9*, 72.